applied sciences

MDPI

Article

Characterizing the As-Fabricated State of Additively Fabricated IN718 Using Ultrasonic Nondestructive Evaluation

Zebadiah Miles [1], Beytullah Aydogan [2], Guillermo Huanes-Alvan [2], Himanshu Sahasrabudhe [2] and Sunil Kishore Chakrapani [1,2,*]

[1] Department of Electrical and Computer Engineering, Michigan State University, East Lansing, MI 48824, USA
[2] Department of Mechanical Engineering, Michigan State University, East Lansing, MI 48824, USA
* Correspondence: csk@msu.edu

Abstract: This article reports on the characterization of the "as-fabricated" state of Inconel 718 samples fabricated using laser directed energy deposition (DED). Laser-DED is known to produce complex metastable microstructures that can significantly influence the baseline ultrasonic response compared to conventional processing methods. The present work uses three parameters to characterize the samples: (a) ultrasonic velocity, (b) an attenuation coefficient, and (c) a backscatter coefficient. The baseline ultrasonic response from the DED sample was compared against the ultrasonic properties of conventional IN718 samples reported in the literature. The results suggest that strong grain boundary scattering from large macrograins can lead to attenuation and backscatter values that are significantly higher than conventional samples. Additionally, the results including velocities, attenuation and backscatter coefficients were found to be dependent on the fabrication direction, with the build direction being different from the transverse directions. Finally, destructive analysis was used to develop conjectures to explain the experimentally observed ultrasonic response.

Keywords: additive manufacturing; ultrasonics; nondestructive evaluation; Inconel 718; material characterization; ultrasonic velocity; ultrasonic attenuation

Citation: Miles, Z.; Aydogan, B.; Huanes-Alvan, G.; Sahasrabudhe, H.; Chakrapani, S.K. Characterizing the As-Fabricated State of Additively Fabricated IN718 Using Ultrasonic Nondestructive Evaluation. *Appl. Sci.* **2023**, *13*, 8137. https://doi.org/10.3390/app13148137

Academic Editor: Mário João S. F. Santos

Received: 10 June 2023
Revised: 30 June 2023
Accepted: 1 July 2023
Published: 13 July 2023

1. Introduction

Laser directed energy deposition (Laser-DED) is an additive manufacturing (AM) technique in which feedstock materials can be fed in powdered form and deposited on metallic substrates using focused laser energy [1–3]. DED machines are capable of high deposition rates, can add and subtract material (hybrid) in the same operation, and develop multi-functional, multi-materials structures [4,5] in a near single step operation [6–8]. Laser-based AM processes such as DED have cooling rates in the range of 10^3 to 10^5 K/s, and are known to produce metastable phases and microstructural features such as fine dendrites, nano-scaled precipitates, acicular grains, etc. [9,10]. Furthermore, the laser-processed microstructure depends a great deal on the material system. For example, in DED fabricated Inconel 718 (IN718) alloy, Laves phases rich in Nb and Mo form a unique striated and segregated network in a γ-phase-rich matrix [9]. Grain boundary segregation of precipitates give rise to features spread over multiple length scales; cellular meso-grains, and nano-scale carbide precipitates. Further, a previously solidified track of metallic material is also subjected to a secondary heating and cooling during layer-wise fabrication of a bulk component during the laser DED process [11,12]. Due to the finite width of the laser scanning track (a hatch scan) and the laser scanning depth (a layer), the laser DED process essentially leads to rapid micro-casting of the metallic material. Currently, material characterization and quality control is performed mostly using destructive techniques [13], which are not always feasible for rapid, in-field testing.

Nondestructive evaluation (NDE) allows us to perform material characterization without the need for any destructive testing. Several NDE methods [14,15] including

ultrasonic testing (UT) [16–21] and X-ray micro computed tomography (CT) [22–25] have been explored. The field implementable nature of UT makes it highly attractive and gives it an edge over radiography. Recent advances in additive technology including process parameter optimization have helped in establishing processing parameters that give a good starting point for quality control. This would typically eliminate any large defects, such as macro-cracking in the as-fabricated state. Considering these factors, microstructural changes and small-scale defects that do not affect the fabrication are typically found to be challenging to inspect. Applying NDE techniques to inspect these structures would produce a baseline NDE response, i.e., the "as-manufactured" state or the "initial state". Based on in-service activities such as fatigue loading, this initial state can evolve from microstructural changes including phase evolution, etc., to macroscale changes including crack growth, which is typically defined as a "damage state". This is a relative term and a clear definition is dependent on application and structure. Fundamentally, the ability to discern between initial state and damage state from an inspection or NDE perspective depends on the damage-feature size and the ability of the technique to resolve this feature. Therefore, it is very important to understand the baseline UT response for quality control of the structures fabricated using any advanced manufacturing techniques. If the baseline response is misunderstood as a damage state, then it could lead to several false positives. Furthermore, there is lot of interest in going towards in situ characterization, while the structures are being fabricated. But it is important to first understand the initial state in an ex situ manner. Therefore, it is important to first address and understand the baseline response from these complex microstructures before addressing the inspectibility of these structures. Specifically, nickle-based super alloys such as IN718 are used for critical applications like gas turbine blades, aircraft engines, etc., where safety is the highest priority, and addressing false positives or negatives are critical for NDE. Developing standards for inspection such as ASTM E3166-20e1 [26], is dependent on the ability to consistently measure the baseline response and use it to differentiate between defects.

Among all the NDE methods, ultrasonic testing is one of more favorable techniques due its volumetric assessment, and its sensitivity to features spread within the bulk–micro length scale. Three parameters are typically used in ultrasonic testing: ultrasonic velocity, attenuation and backscatter. The ultrasonic velocity of a sample is dependent on the elastic properties of the constituents including phases and other inclusions [27–29]. The attenuation in a material and velocity are related through the dispersion characteristics described by the Kramers–Kronig relationship [30]. The phase velocity is a good indicator of the presence of any microporosity and other scatters as demonstrated earlier by several researchers [31,32]. Similar to the attenuation coefficient, the acoustic energy that is scattered from grains and inclusions and picked up by the transducer is characterized by the backscatter coefficient. The backscatter coefficient has been used to obtain a quantitative and qualitative measure of grain size [33,34], influence of multiple phases and the morphology of grains including elongated grains [35].

Most of the existing studies in literature on ultrasonic NDE have focused on characterizing samples made using powder bed fusion (PBF) and only a handful of articles have focused on laser DED [36–39]. Ultrasonic wave propagation in complex metastable structures (like DED processed structures) is relatively unknown and poorly understood. The objective of the present study is to use UT to characterize the as-fabricated state of IN718 fabricated via laser DED process. This article reports on the use of three parameters to characterize DED processed IN718 structures: (a) ultrasonic velocity, (b) an attenuation coefficient, and (c) a backscatter coefficient. We further compare the baseline ultrasonic properties of the DED samples to the ultrasonic properties of conventional IN718 sample reported in literature. Conjectures were developed based on the observations on the velocity, attenuation and backscatter coefficient based on known theories. To the authors' knowledge, this is the first comprehensive work that reports on all the ultrasonic properties of DED processed IN718. Therefore, the focus of the article is only on the nondestructive characterization and developing conjectures.

2. Materials and Methods

2.1. Materials

DED IN718 structures were fabricated using a Laser Engineered Net Shaping (LENS™) directed energy deposition machine. The processing parameters using to fabricate the DED samples are listed in Table 1. Since the aim of the study is not processing parameter optimization, the parameters that were optimized previously by a commercial supplier, Optomec Inc. Alburquerque, New Mexico, USA, were used. These processing parameters were identified for high deposition rates with no significant defects, which was also verified with destructive analysis. The same processing parameters were used to fabricate more than three samples and were found to be consistent using destructive analysis as reported earlier by the authors [40]. A zigzag scanning pattern was used with alternating 0° to 90° in between layers during fabrication. The samples were deposited to a near net-shaped cubic geometry on a 12 mm thick stainless steel 304 base plate. The samples were further cut from the base plates and milled to a final dimension of 25 mm (L) × 25 mm (W) × 19 mm (H) sample, with the height being the build direction thickness as shown in Figure 1a. The sample surfaces were milled flat to a surface roughness, which is approximately equivalent to an asperity height of $Ra < 0.25$. The Archimedes method was used to measure the density of the sample: 8248 kg/m^3 and the expected density was 8220 kg/m^3. Observations from microscopy and destructive measurements did not show any significant porosity. The details of the setups used for destructive testing can be found elsewhere [40].

Table 1. Process parameters used in the present study.

Parameter	Value
Oxygen and moisture	<20 ppm
Laser power	1000 W
Speed	14.4 mm/s
Powder feed rate	12.3 g/min
Powder particle size	16–44 µm

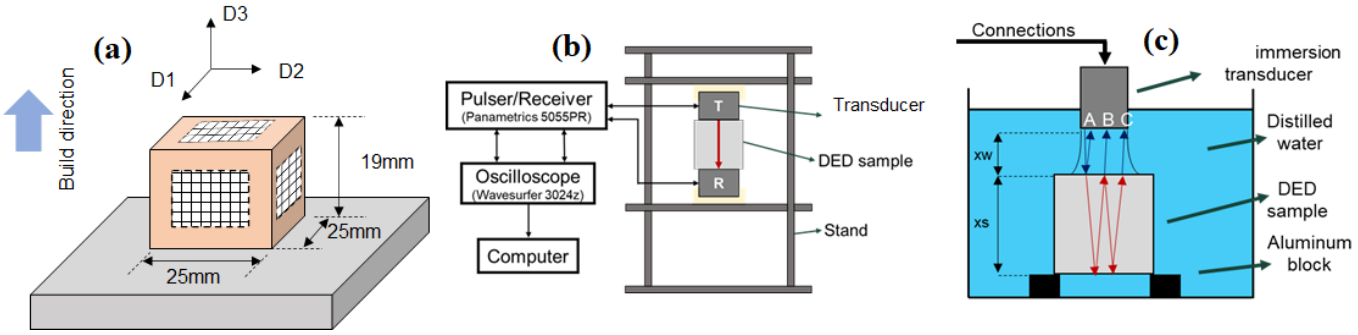

Figure 1. (**a**) Sample geometry after machining, D3 is the build direction. The hatched region shows the 300 mm^2 region where all the ultrasonic measurements were carried out on each face of the sample. (**b**) The through-transmission setup that was used for velocity measurement. (**c**) The immersion setup that was used for attenuation and backscatter coefficient measurement. A, B, C refer to the frontwall, backwall and 2nd backwall. For the backscatter measurements, a focused transducer was used.

2.2. Ultrasonic Characterization

2.2.1. Phase and Group Velocity

The longitudinal group velocities were measured using a contact-based transducer (Olympus) in pulse-echo setup [41]. The transducer frequency was 5 MHz and the active area was 12 mm (0.5 inch). The shear group velocities were measured using two transducers in the through transmission ultrasound (TTU) setup as shown in Figure 1b. The shear transducer frequency was 2.25 MHz and the active area was 12 mm (0.5 inch). A mass loaded setup was used to obtain consistent loading pressure, which reduces the measurement error. Five measurements were carried out along each principal direction of the sample by

moving the transducer within a 300 mm^2 region. This region was chosen at the center of the sample as shown in hatched region in Figure 1a to ensure no edge effects interfered with the measurements. Data capture was carried out at 1GHz using an 8-bit oscilloscope, and a Panametrics 5055 pulser-receiver. The group velocities were calculated using the time of flights of the two backwall echoes, which were extracted from the recorded waveforms using Hilbert transforms. The same approach was used for shear velocity measurements, except for a fused silica reference, which was used to obtain the time of flight difference in the TTU setup. More details can be found in the supplementary material.

The phase velocity as a function of frequency was obtained using the procedure outlined in Ref. [32]. Typically, the phase velocity in the 5–15 MHz range for metallic structures will be invariant of the frequency [42]. Therefore, we used a 1 MHz, 12 mm (0.5 inch) diameter transducer in pulse-echo mode to capture the phase velocity in the 0.1 MHz to 2.5 MHz range. Three measurements were carried out along each principal direction of the sample by moving the transducer within a 300 mm^2 region, and the response was averaged. More details of the phase velocity measurement are given in the supplementary material. The experimental setup is similar to Figure 1b, albeit using only one transducer instead of two.

2.2.2. Attenuation Coefficient

The method to measure the attenuation coefficient (α) is given in the supplementary text and follows Ref. [43]. An immersion setup as shown in Figure 1c is part of a 3-axis scanner controlled by InspectionWare software, which was used for data collection. A 5 MHz, 6 mm (0.25 inch) diameter planar immersion transducer was used in pulse-echo mode. The Panametrics 5055 pulser-receiver was used along with a 12-bit digitizer with a sampling rate of 250 MHz. The data were collected via InspectionWare, then processed in MATLAB using custom written codes. The front wall (FW) and first backwall (BW) were used to calculate the attenuation coefficient. The α was also measured for different directions to obtain the effect of the build direction and three measurements were carried out within a 300 mm^2 region.

2.2.3. Backscatter Coefficient

The procedure for backscatter coefficient measurement is given in the supplementary text and follows Refs. [43,44]. The measure of the noise generating capacity of the microstructure is given by the Figure of Merit (FOM). A 5 MHz, 12.7 mm (0.5 inch) transducer with 101 mm (4 inch) focus in water was used for the backscatter measurement. A 10 mm $\times$ 10 mm C-Scan with a 500 µm spatial resolution (position around the geometric center of the face of the sample) focused at the mid-plane of the sample was carried out along the three different directions. The experimental setup is similar to Figure 1c, with the exception of the focused transducer. Signal processing was carried out with careful time gating of the signal between the frontwalls and backwalls. The transducer was positioned with the focal spot at the surface of the sample, and the FW signal was captured and used as the reference. More details of various corrections and the equation can be found in the supplementary.

3. Results

3.1. Velocity

3.1.1. Group Velocities

The measured longitudinal group velocities of the DED sample are shown in Figure 2a. As a reference, the longitudinal velocity of conventional IN718 from [45] has been plotted in a dashed line. It is apparent that the longitudinal velocities of the DED sample are lower than the conventional sample. Furthermore, a dependence on the direction can also be noticed, i.e., the build direction (D3) shows the lowest velocity, followed by D2 and D1. The shear group velocities are shown in Figure 2b. The velocity D1-2 signifies propagation along direction 1 and polarization along 2. Compared to conventional values, the DED

sample has a higher velocity in the D1-3 and D2-3 directions, but the transverse plane, i.e., D1-2, exhibits lower velocity than the conventional sample. This suggests that the build direction of D3 has a significant influence on the shear properties.

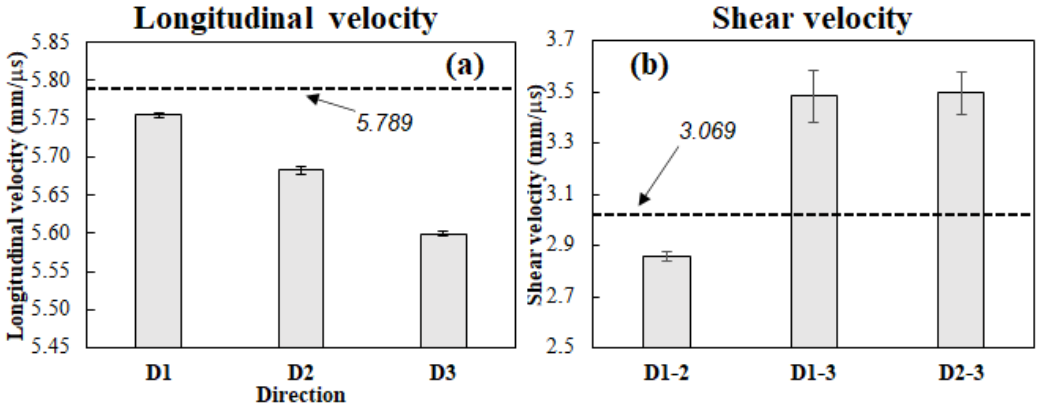

Figure 2. (**a**) Longitudinal group velocity along the three directions, (**b**) shear group velocity along the three directions. D1-2 refers to propagation along 1 and polarization along 2. D3 is the build direction. For reference, the longitudinal and shear velocities of conventional IN718 [45] have been added as dashed lines.

3.1.2. Phase Velocity

The longitudinal phase velocities along the three directions are shown in Figure 3. According to Kramer–Kronig [32] relationship, an inverse-asymptotic behavior is expected between phase velocity and frequency. The shape of the phase velocity curve is consistent with previously published data for high attenuation samples including polymer composites [32]. The dispersion, i.e., frequency dependence of phase velocity signifies the dependence on attenuation including porosity and other features. Between the different directions, the DED sample shows strong dispersion and the build direction; D3 shows a higher dispersion compared to D1 and D2.

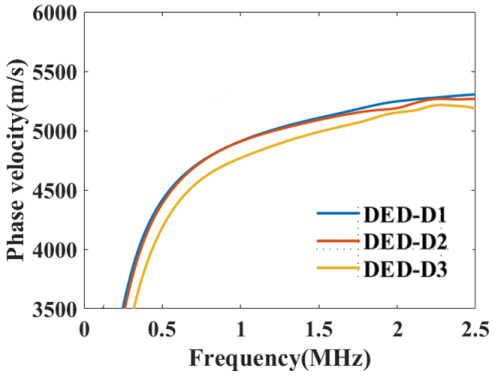

Figure 3. Phase velocity vs. frequency comparing the three directions of the DED sample. D3 is the build direction.

3.2. Attenuation Coefficient

The raw A-Scan data are shown in Figure 4. The reference frontwall echo is shown in Figure 4a and the received first backwall signal for D1 and D3 are shown in Figure 4b,c. The frequency domain response of the FW, and BW of D1, D3 are shown in Figure 4d–f. Since the received signal has a total bandwidth of ≈2–7 MHz, we limit our analysis to this range. A bi-modal spectral distribution can be observed in the spectral response. Interestingly, the bimodal response is not as sharp for D3 compared to D1. The calculated α values are shown in Figure 5. The three measurements per direction have been plotted together in lighter shade and the average value is shown in a darker shade. At 5 MHz, the DED

sample exhibits ≈0.5 Np/cm, compared to the conventional sample ≈0.0025 Np/cm [46]. For 50 mm of propagation, this will result in ≈22 dB difference between conventional sample and DED sample, which is significant. Furthermore, beyond the 7 MHz range, we can observe a periodic noise (in the shaded region in Figure 5), which is due to the convolution noise. The bandwidth outside our analysis is shown in the light red region and is not considered in the work. Within the 2–7 MHz range, we can observe "humps" or "peaks". These humps seem to occur at specific frequencies and seem to be dependent on the direction. The D1 and D2 results show that the humps occur at or near the same frequency, i.e., 3.5 MHz, but for D3, we notice this hump is not as sharp and is closer to 4 MHz. The origin of these humps and their physical relevance to the ultrasonic measurements will be discussed in Section 4.

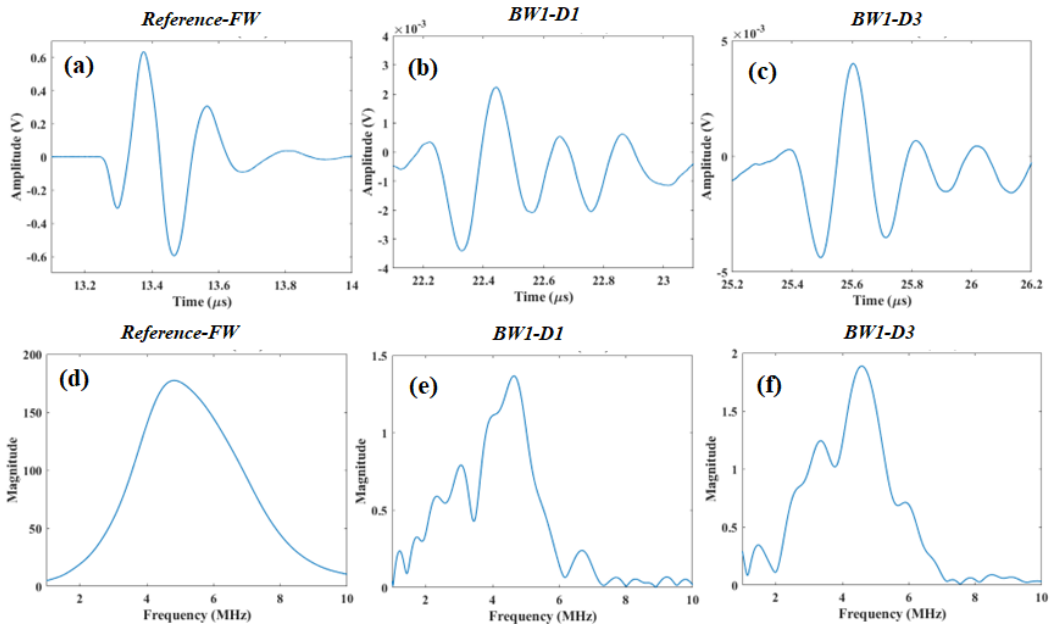

Figure 4. The raw A-Scan data used for calculating the attenuation parameter (α) are shown. The time domain response of (**a**) reference front wall (FW) echo, (**b**) backwall1 (BW1) along D1 and (**c**) BW1 along D3. The corresponding spectral response is shown for (**d**) FW, (**e**) BW1 along D1 and (**f**) BW1 along D3. D3 is the build direction.

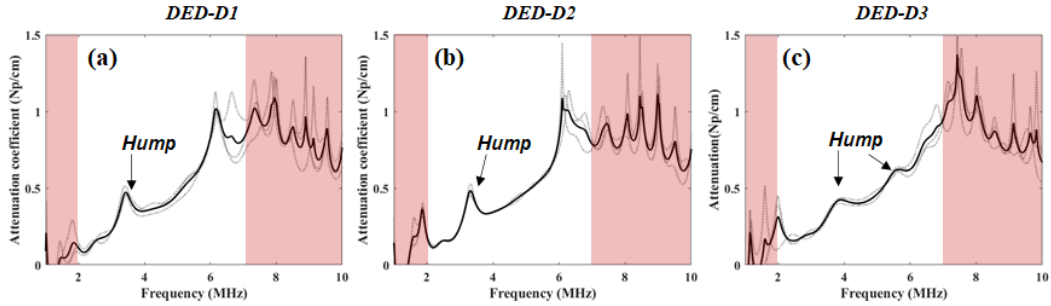

Figure 5. Attenuation parameter (α) of the DED sample with waves propagating along (**a**) D1, (**b**) D2 and (**c**) D3 directions. D3 is the build direction.

3.3. Backscatter Coefficient

The raw A-Scan data are shown in Figure 6. The time-domain reference fontwall echo and the backscatter region of D1 and D3 are shown in Figure 6a–c. The frequency-domain response of the signals in Figure 6a–c are shown in Figure 6d–f. Since the attenuation coefficient was used to calculate the backscatter coefficient, we limit the bandwidth to 2–7 MHz as well. Similar to attenuation, the bandwidth outside our analysis is shown in the light red region and is not considered in the work. An example of the backscatter region

in time domain along D1 and D3 are shown in Figure 6c,d. The backscattered signal has a higher amplitude along D3 compared to D1. The backscatter spatial RMS magnitude (Γ_{rms}) is shown in Figure 6e,f. The periodic grain noise along D3 manifests as a strong peak in Γ_{rms}. The calculated FOM values are shown in Figure 7. Between 4–5 MHz, the FOM is 0.0025 $cm^{-0.5}$, whereas, between 5–6 MHz, it is ≈0.0225 $cm^{-0.5}$ for D3 and ≈0.01 $cm^{-0.5}$ for D2. The FOM values reported in literature for conventional IN718 at 5 MHz is between 0.003–0.005 $cm^{-0.5}$ [34]. It is interesting to note that below 5 MHz for the DED samples, the grain noise is similar to conventional structures; however, the strong periodic noise results in a FOM that is an order of magnitude larger.

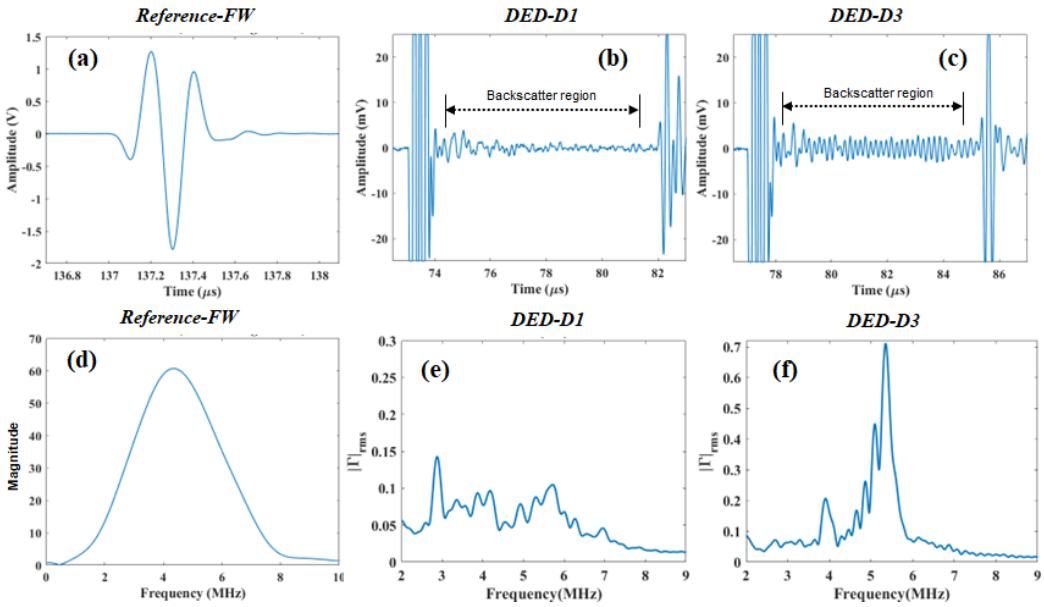

Figure 6. The raw A-Scan data used for calculating the FOM are shown. The time domain response of (**a**) reference front wall (FW) echo, (**b**) backscatter region along D1 and (**c**) backscatter region along D3. The corresponding spectral response is shown in for (**d**) FW, (**e**) frequency domain response of spatial RMS magnitude (Γ_{rms}) along D1 and (**f**) Γ_{rms} along D3. D3 is the build direction.

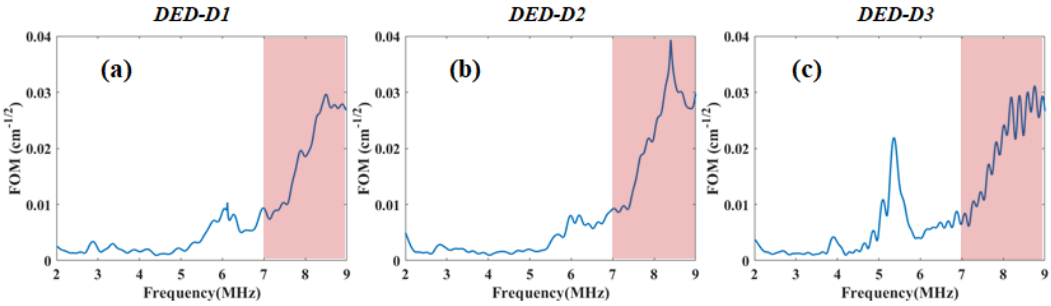

Figure 7. FOM as a function of frequency of the DED sample measured along (**a**) D1, (**b**) D2 and (**c**) D3 directions. D3 is the build direction.

3.4. Backscatter C-Scan to Map Heterogeneity

To obtain a qualitative measure of the spatial heterogeneity, the DED sample was scanned using a 2-axis scanner and the same setup as the backscatter measurement. Compared to the backscatter measurement, the entire sample was scanned at a spatial resolution of 500 µm in both scan and index directions. A backscatter C-Scan was developed by focusing at the mid-plane of the sample, and isolating the time-domain signal at the focus using a 2 µs gate. The time-domain signals were further converted into frequency domain, and a sum of the absolute magnitude in the frequency domain was carried out. This will result in a single value at each pixel, and repeating this process over the entire scan area will

result in what is referred to as a backscatter C-Scan as shown in Figure 8. Since the main objective is to only capture the intra-sample heterogeneity, the amplitudes were normalized and plotted in dB scale as shown in the figure. It is interesting to note that the heterogeneity in D1 as shown in Figure 8a only shows a −5 dB variation in spatial amplitude, but D2 and D3 as shown in Figure 8b,c show up to −10 dB in spatial variability.

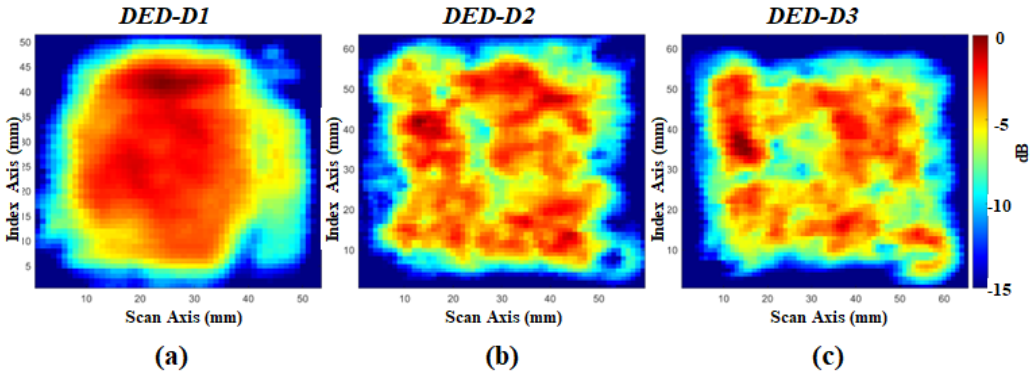

Figure 8. Backscatter C-Scan of the sample from different directions; (**a**) D1, (**b**) D2 and (**c**) D3. The ultrasonic beam was focused at the mid-plane of the sample. The spatial heterogeneity can be observed in the amplitude.

4. Discussion

The objective of this article is to understand the complex ultrasonic response of the as-fabricated IN718 sample, which will allow us to eventually develop models that can quantify the as-fabricated state from a microstructral perspective. This will also allow us to differentiate the as-fabricated state with defect state, which is critical for qualification using ultrasonic NDE.

4.1. Destructive Measurements

After the NDE measurements were carried out, the DED sample was sectioned, polished and micrographed. The micrographs of the DED sample are shown in Figure 9 along with a reference micrograph of conventional IN718. In the conventional sample in Figure 9a, the grains are somewhat equiaxed and show a uniform grain size distribution. The presence of Laves phases (white outlines in the grain boundaries) can also be observed, which is once again consistent with known microstructures. Figure 9b,c shows the DED sample in the X-Y and Z planes. We can observe the following: (i) micro- and macrocolonies of grains with non-uniform grain size distribution, (ii) dendritic or long slender grains [47], and (iii) strong grain boundary precipitation of metastable Laves phases [48]. A separate phase analysis was also carried out using X-Ray diffraction (XRD) and details are reported elsewhere [40]. The phase distribution was found to be similar between the conventional and DED structures. However, in the DED structure, the γ'' phase of Ni_3Nb did not precipitate due to the rapid solidification and segregation of Nb as Laves phases [40]. These micrograph scales were chosen to show the "macrograins". At the micrograin scale in Figure 9b, a network of connected white lines resembling a cellular structure can be observed. At the lower magnification in Figure 9c, the larger macrograins become visible (as outlined in orange).

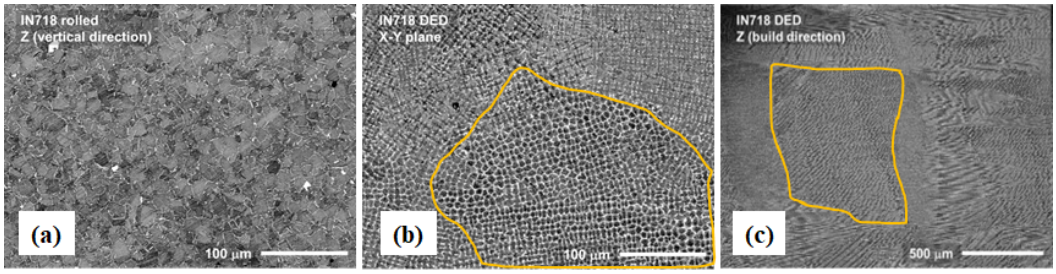

Figure 9. Micrographs of (**a**) Z plane of conventional sample, (**b**) X-Y plane of DED sample, and (**c**) Z plane of DED sample.

4.2. Velocities

We can observe that the longitudinal velocity of the DED sample is lower than conventional samples. We can hypothesize that one of the reasons for the difference in velocity between conventional and DED samples could be due to the lack of γ'' phase in the DED sample. This could also be partly attributed to the wide distribution of carbide phases, which are known to have a lower modulus [49,50]. As noted in Section 4.1, previous destructive analysis had shown that the DED IN718 sample had a higher volume fraction of Laves phases and a lower volume fraction of γ'' phases [40]. Previous work on aging of IN718 [45] shows that IN718 samples without the γ'' phase exhibited lower longitudinal and shear velocities compared to the sample with the γ'' phase. The hypothesis that the lack of γ'' in the DED-IN718 sample will decrease the velocity agrees well with the present observations for the longitudinal velocities. Metallography of the present samples [40] also showed a large distribution of carbide phases, which once again agrees with the hypothesis of reduction in velocity for DED samples.

The shear velocity in the transverse direction D1-2 is also lower than the conventional sample, which once again is in good agreement with previous observations [45]. However, the shear velocities of the DED sample are higher than the conventional sample along the build direction (D1-3 and D2-3), which is contrary to the hypothesis. The velocity shows some degree of anisotropy, which points towards texture. However, to fully understand it, an electron backscatter diffraction (EBSD) analysis is needed, which is beyond this article. Other articles have carried out similar analyses for IN625 but using powder bed fusion rather than DED [51].

4.3. Grain Clusters and Scattering

From the attenuation measurements in Figure 5, we can observe a hump at 3.5 MHz in D1, D2 and at 4 MHz in D3. Similarly a hump at 4 MHz and 5 MHz can be observed in the FOM results in Figure 7. A hypothesis for this hump is presented below: (A) The 22 dB difference in attenuation between conventional sample and DED sample suggests, the average grain size must be significantly larger in the DED sample. From the micrographs in Figure 9, we can notice that the macrograins are spread between 100–500 µm, whereas conventional samples typically have grain sizes on the order of 10–20 µm. The micrograins on the other hand are on the order of 5–10 µm. Based on these observations, it can be argued that the scattering and attenuation observed in the DED sample can be mainly due to the macrograin. For the macrograin to act as a single grain, the assumption is that the macro-grain has a local texture, which has been shown earlier by other authors using EBSD imaging [52]. (B) For conditions when the scatterer size is approximately equal to the wavenumber, i.e., $ka = 1$, where k is wavenumber and a is the average scatterer size, Stanke and Kino [53] have shown that a transition in the scatter mechanism from Rayleigh to stochastic occurs. The power law of frequency dependence also changes at this transition according to S-K theory. Depending on various factors, a hump can be observed [54,55] at this transition. The reason for the hump like behavior can be due to grain size distribution [54], or grain morphology [55]. If the hump observed at 3.5 MHz is a transition, then $ka = 1$ will give us an average grain diameter of ≈250–300 µm based

on S-K theory. From the micrographs in Figure 9, this macrograin size is possible. If the grain scattering were to occur from the micrograin, then the transition is expected around hundreds of MHz-GHz, which is not feasible with the current setup.

There could be a few arguments that can be made against this hypothesis as well: It is interesting to note that there is no change in power law dependence before and after the 3.5 MHz hump, which is expected for a transition based on S-K theory. Furthermore, the forward scatter noise overlapping the backwall could also result in aberrations in the spectral response. This will typically result in bi-modal spectrum as shown in Figure 4d,e, and taking the ratio of this spectrum with a smooth spectrum like the reference (in Figure 5b) will result in humps. Any local velocity changes will also result in phase aberrations as the beam propagates. Therefore, it could also be argued that these humps are purely spectral aberrations due to time-gating or the choice of time gate position. The origin of the humps remains debatable and uncertain and further work is necessary to understand them completely.

4.4. Heterogeneity

Adapting the existing acoustic scattering theories to complicated DED microstructures will be challenging due to two reasons: (a) the spatial heterogeneity, and (b) grain size definition. The C-Scans in Figure 8 suggest that the spatial variability/heterogeneity is much more significant in the DED sample compared to the conventional sample. This variability calls into question the fundamental definition of attenuation and backscatter coefficients, especially for heterogeneous structures. The acoustic parameters which are used to calculate the attenuation and backscatter coefficients such as velocity, diffraction correction, etc., are dependent on homogeneous assumptions. These properties are typically averaged over the beam volume. The C-Scans suggest that we may not be able to use the standard definitions of attenuation and backscatter coefficients to characterize DED samples.

Secondly, the definition of grain in these complex microstructures is not consistent in the literature. To correlate the results with scattering theories, we need to perform mean free path calculations [43,56], which requires us to clearly define grain morphology. Unfortunately, there seems to be no clear consensus in the additive manufacturing/DED research community on the definition of a grain size for meta-stable microstructures [57–62]. Specifically for IN718, the segregation of Laves phase at the grain boundaries results in a cellular microstructure. If we assume the cell is the grain, then based on average cell size, the grain size will 5–10 µm, and if we define the grain to be the macrocolony of cells, then the average grain size will be ≈250–500 µm. The macrograin definition seems to agree well with the results presented here. However, more research is needed from an acoustic perspective to determine the appropriate scattering functions for the corresponding grain size.

4.5. Absorption and Residual Stress

There are several sources of attenuation that are independent of grain boundary scattering such as thermoelastic attenuation, lattice defects like dislocations, grain boundaries and inclusions like precipitates. Literature suggests that thermoelastic attenuation is typically orders of magnitude smaller [63] than grain boundary scattering, and therefore we can discount its effects. Attenuation due to dislocation damping scales quadratically with the frequency. This effect is higher at lower frequencies, and minimal above 10 MHz [64]. Based on the Granato–Lucke model [65], attenuation scales to the fourth power of the dislocation loop length ($\propto L^4$) and linear to the dislocation density. Based on the micrographs, we can hypothesize that the relatively small cell size might result in smaller dislocation loop lengths and therefore a smaller dislocation damping contribution. However, the dislocation density within the cells can be higher for the DED samples, which needs to be experimentally validated.

The rapid solidification can result in long-range and short-range residual stresses and texture in the structure [66]. This is expected to manifest in the ultrasonic velocity due to acoustoelasticity, i.e., stress-induced velocity changes [67]. In Figure 2a,b, we can observe that the longitudinal velocity and shear velocities along the build directions are different compared to the transverse direction. The presence of texture and residual stress can contribute directly to the anisotropy [51]. This suggests that more studies are needed to fully understand the contributions to ultrasonic velocity in DED structures.

5. Summary

The objective of this article is to characterize the ultrasonic properties of the as-fabricated state of additively manufactured IN718 structures. Samples were fabricated using DED technique, and three parameters; ultrasonic velocity, and attenuation and backscatter coefficients; were measured in the as-fabricated state, i.e., no post-processing or heat treatments. This forms the baseline ultrasonic response of DED structures, which were compared with the conventional IN718 reported in the literature. The purpose of the ex situ measurements reported here is to highlight the importance of first understanding the baseline ultrasonic response before we develop in situ characterization, i.e, inspection while the structures are being fabricated. The results and observations from this study are summarized below:

- The ultrasonic velocity shows that the DED sample exhibits a noticeable anisotropy compared to the conventional sample. Specifically, the build direction has a large influence on the ultrasonic velocities. The DED sample has a lower longitudinal velocity compared conventional samples, which could possibly be attributed to the lack of γ'' phase. However, the transverse shear velocity along the D1-2 plane was higher than conventional sample, which is conflicting with the hypothesis.
- The DED sample exhibits significantly higher attenuation (-22 dB) compared to conventional sample, and the presence of humps were observed. The origin of these humps in the attenuation curve are debatable and presently there is no explanation.
- Ultrasonic backscatter results also suggest that the DED sample exhibits higher ultrasonic backscatter compared to conventional sample. Due to the periodic noise, strong peaks could be observed at certain frequencies. However, outside that frequency range, the FOM values are similar to conventional samples. The backscatter along the build direction was noticeably higher than the transverse directions.
- Heterogeneity: The DED sample shows a -10 dB spatial variability in amplitude, which is considerable compared to conventional samples. It was also observed that this heterogeneity might be dependent on direction.

The high attenuation and strong backscatter suggest that the as-fabricated sample could easily be mistaken for a defective sample. This poses a strong challenge when we use ultrasonic NDE to study the influence of processing parameters or other factors. If the as-fabricated state cannot be understood, any changes in the ultrasonic response based on the changes in processing parameters cannot be understood either. This becomes a major roadblock in moving towards a NDE-based qualification of these structures. The heterogeneity observed in the DED sample can be a major hurdle in developing qualification standards for DED samples. However, the attenuation and backscatter measurements are rich with information that we currently do not understand. Extracting more features from these measurements could possibly allow us to develop more advanced qualifications compared to the existing qualification tools, which use velocity, attenuation and backscatter coefficients. Such an exercise will be explored elsewhere. Finally, we do not believe these observations can be generalized for all metallic structures that are fabricated using DED. These observations maybe specific to IN718 and other structures which have grain boundary precipitation and meta-stable martensitic phases in their microstructure. The results also suggest that more research is required to fully understand the origins of the baseline ultrasonic response, especially wave propagation in complex microstructures.

Supplementary Materials: The following supporting information can be downloaded at: https://www.mdpi.com/article/10.3390/app13148137/s1, Reference [68] are cited in the supplementary materials.

Author Contributions: Conceptualization, S.K.C.; Methodology, Z.M., B.A. and H.S.; Formal analysis, Z.M., B.A. and G.H.-A.; Investigation, Z.M. and G.H.-A.; Resources, H.S. and S.K.C.; Data curation, Z.M.; Writing—original draft, S.K.C., Z. M; Writing—review & editing, Z.M., B.A. and H.S.; Supervision, H.S. and S.K.C.; Project administration, S.K.C. All authors have read and agreed to the published version of the manuscript.

Funding: B. Aydogan is grateful for the financial support from the Republic of Turkey to pursue a Ph.D. program in the USA.

Institutional Review Board Statement: Not applicable.

Informed Consent Statement: Not applicable.

Data Availability Statement: Data will be made available on request by contacting Sunil K. Chakrapani.

Conflicts of Interest: The authors declare no conflict of interest.

Abbreviations

The following abbreviations are used in this manuscript:

DED	Directed Energy Deposition
IN718	Inconel 718
AM	Additive Manufacturing
NDE	Nondestructive Evaluation
UT	Ultrasonic Testing
TTU	Through Transmission Ultrasound
FW	Front Wall
BW	Back Wall
FOM	Figure Of Merit

References

1. Askari, M.; Hutchins, D.A.; Thomas, P.J.; Astolfi, L.; Watson, R.L.; Abdi, M.; Ricci, M.; Laureti, S.; Nie, L.; Freear, S.; et al. Additive manufacturing of metamaterials: A review. *Addit. Manuf.* **2020**, *36*, 101562. [CrossRef]
2. Thompson, S.M.; Bian, L.; Shamsaei, N.; Yadollahi, A. An overview of Direct Laser Deposition for additive manufacturing; Part I: Transport phenomena, modeling and diagnostics. *Addit. Manuf.* **2015**, *8*, 36–62. [CrossRef]
3. Svetlizky, D.; Das, M.; Zheng, B.; Vyatskikh, A.L.; Bose, S.; Bandyopadhyay, A.; Schoenung, J.M.; Lavernia, E.J.; Eliaz, N. Directed energy deposition (DED) additive manufacturing: Physical characteristics, defects, challenges and applications. *Mater. Today* **2021**, *49*, 271–295. [CrossRef]
4. Chen, D.; Zheng, X. Multi-material additive manufacturing of metamaterials with giant, tailorable negative Poisson's ratios. *Sci. Rep.* **2018**, *8*, 9139. [CrossRef]
5. Sahasrabudhe, H.; Harrison, R.; Carpenter, C.; Bandyopadhyay, A. Stainless steel to titanium bimetallic structure using LENS™. *Addit. Manuf.* **2015**, *5*, 1–8. [CrossRef]
6. Chen, Y.; Zhang, X.; Parvez, M.M.; Liou, F. A review on metallic alloys fabrication using elemental powder blends by laser powder directed energy deposition process. *Materials* **2020**, *13*, 3562. [CrossRef] [PubMed]
7. Feenstra, D.; Molotnikov, A.; Birbilis, N. Effect of energy density on the interface evolution of stainless steel 316L deposited upon INC 625 via directed energy deposition. *J. Mater. Sci.* **2020**, *55*, 13314–13328. [CrossRef]
8. Dass, A.; Moridi, A. State of the art in directed energy deposition: From additive manufacturing to materials design. *Coatings* **2019**, *9*, 418. [CrossRef]
9. Aydogan, B.; Sahasrabudhe, H. Effects of Heat Treatment on Direct Laser Fabricated Stainless Steel 420-Inconel 718 Alloy Multi-material Structures. *J. Mater. Eng. Perform.* **2022**, *31*, 9802–9811. [CrossRef]
10. Zhang, Y.; Bandyopadhyay, A. Influence of compositionally graded interface on microstructure and compressive deformation of 316L stainless steel to Al12Si aluminum alloy bimetallic structures. *ACS Appl. Mater. Interfaces* **2021**, *13*, 9174–9185. [CrossRef]
11. Singh, A.K.; Mundada, Y.; Bajaj, P.; Wilms, M.B.; Patil, J.P.; Mishra, S.K.; Jägle, E.A.; Arora, A. Investigation of temperature distribution and solidification morphology in multilayered directed energy deposition of Al-0.5 Sc-0.5 Si alloy. *Int. J. Heat Mass Transf.* **2022**, *186*, 122492. [CrossRef]
12. Joshi, S.S.; Sharma, S.; Mazumder, S.; Pantawane, M.V.; Dahotre, N.B. Solidification and microstructure evolution in additively manufactured H13 steel via directed energy deposition: Integrated experimental and computational approach. *J. Manuf. Process.* **2021**, *68*, 852–866. [CrossRef]

13. Lewandowski, J.J.; Seifi, M. Metal additive manufacturing: A review of mechanical properties. *Annu. Rev. Mater. Res.* **2016**, *46*, 151–186. [CrossRef]
14. Honarvar, F.; Varvani-Farahani, A. A review of ultrasonic testing applications in additive manufacturing: Defect evaluation, material characterization, and process control. *Ultrasonics* **2020**, *108*, 106227. [CrossRef] [PubMed]
15. Mandache, C. Overview of non-destructive evaluation techniques for metal-based additive manufacturing. *Mater. Sci. Technol.* **2019**, *35*, 1007–1015. [CrossRef]
16. Slotwinski, J.A.; Garboczi, E.J. Porosity of additive manufacturing parts for process monitoring. *Am. Inst. Phys.* **2014**, *1581*, 1197–1204.
17. Rieder, H.; Spies, M.; Bamberg, J.; Henkel, B. On-and offline ultrasonic characterization of components built by SLM additive manufacturing. In *Proceedings of the AIP Conference Proceedings*; AIP Publishing LLC: Melville, NY, USA, 2016; Volume 1706, p. 130002.
18. Kim, C.; Yin, H.; Shmatok, A.; Prorok, B.C.; Lou, X.; Matlack, K.H. Ultrasonic nondestructive evaluation of laser powder bed fusion 316L stainless steel. *Addit. Manuf.* **2021**, *38*, 101800. [CrossRef]
19. Wang, X.; Li, W.; Li, Y.; Zhou, Z.; Zhang, J.; Zhu, F.; Miao, Z. Phased array ultrasonic testing of micro-flaws in additive manufactured titanium block. *Mater. Res. Express* **2020**, *7*, 016572. [CrossRef]
20. Bellotti, A.; Kim, J.Y.; Bishop, J.E.; Jared, B.H.; Johnson, K.; Susan, D.; Noell, P.J.; Jacobs, L.J. Nonlinear ultrasonic technique for the characterization of microstructure in additive materials. *J. Acoust. Soc. Am.* **2021**, *149*, 158–166. [CrossRef]
21. Khabouchi, A.; Ventura, P.; Leymarie, N.; Hazotte, A.; Germain, L. Crystallographic texture and velocities of ultrasonic waves in a Ni-based superalloy manufactured by laser powder bed fusion. *Mater. Charact.* **2020**, *169*, 110607. [CrossRef]
22. Du Plessis, A.; Sperling, P.; Beerlink, A.; Du Preez, W.B.; Le Roux, S.G. Standard method for microCT-based additive manufacturing quality control 4: Metal powder analysis. *MethodsX* **2018**, *5*, 1336–1345. [CrossRef] [PubMed]
23. Shen, B.; Li, H.; Liu, S.; Zou, J.; Shen, S.; Wang, Y.; Zhang, T.; Zhang, D.; Chen, Y.; Qi, H. Influence of laser post-processing on pore evolution of Ti–6Al–4V alloy by laser powder bed fusion. *J. Alloys Compd.* **2020**, *818*, 152845. [CrossRef]
24. Shrestha, S.; Starr, T.; Chou, K. Porosity analysis in metal additive manufacturing by micro-ct. *Am. Soc. Mech. Eng.* **2018**, *52019*, V002T02A059.
25. Shrestha, S.; Chou, K. Build location effect on the single-track pore characteristics formed with the laser powder bed fusion process. *Manuf. Lett.* **2021**, *28*, 6–10. [CrossRef]
26. *ASTM Standard E3166-20e1*; Standard Guide for Nondestructive Examination of Metal Additively Manufactured Aerospace Parts After Buildy. ASTM: West Conshohocken, PA, USA, 2020.
27. Gür, C.H.; Cam, I. Comparison of magnetic Barkhausen noise and ultrasonic velocity measurements for microstructure evaluation of SAE 1040 and SAE 4140 steels. *Mater. Charact.* **2007**, *58*, 447–454. [CrossRef]
28. Murthy, G.; Ghosh, S.; Das, M.; Das, G.; Ghosh, R. Correlation between ultrasonic velocity and indentation-based mechanical properties with microstructure in Nimonic 263. *Mater. Sci. Eng. A* **2008**, *488*, 398–405. [CrossRef]
29. Kumar, A.; Shankar, V.; Jayakumar, T.; Rao, K.B.S.; Raj, B. Correlation of microstructure and mechanical properties with ultrasonic velocity in the Ni-based superalloy Inconel 625. *Philos. Mag. A* **2002**, *82*, 2529–2545. [CrossRef]
30. O'Donnell, M.; Jaynes, E.; Miller, J. Kramers–Kronig relationship between ultrasonic attenuation and phase velocity. *J. Acoust. Soc. Am.* **1981**, *69*, 696–701. [CrossRef]
31. Hsu, D.K.; Nair, S.M. Evaluation of porosity in graphite-epoxy composite by frequency dependence of ultrasonic attenuation. In *Review of Progress in Quantitative Nondestructive Evaluation*; Springer: Berlin/Heidelberg, Germany, 1987; pp. 1185–1193.
32. Hsu, D.K.; Jeong, H. Ultrasonic velocity change and dispersion due to porosity in composite laminates. In *Review of Progress in Quantitative Nondestructive Evaluation*; Springer: Berlin/Heidelberg, Germany, 1989; pp. 1567–1573.
33. Panetta, P.D. Backscattering and Attenuation during the Propagation of Ultrasonic Waves in Duplex Titanium Alloys. Ph.D. Thesis, Iowa State University, Ames, IA, USA, 1999.
34. Haldipur, P. *Material Characterization of Nickel-Based Super Alloys through Ultrasonic Inspection*; Iowa State University: Ames, IA, USA, 2006.
35. Lobkis, O.; Yang, L.; Li, J.; Rokhlin, S. Ultrasonic backscattering in polycrystals with elongated single phase and duplex microstructures. *Ultrasonics* **2012**, *52*, 694–705. [CrossRef]
36. Chabot, A.; Laroche, N.; Carcreff, E.; Rauch, M.; Hascoët, J.Y. Towards defect monitoring for metallic additive manufacturing components using phased array ultrasonic testing. *J. Intell. Manuf.* **2020**, *31*, 1191–1201. [CrossRef]
37. Huanes-Alvan, G.; O'Neil, A.; Sahasrabudhe, H.; Chakrapani, S.K. Baseline estimation of ultrasonic response of metallic structures fabricated via laser direct energy deposition (DED). In Proceedings of the QNDE2019-6989 46th Annual Review of Progress in Quantitative Nondestructive Evaluation, Portland, OR, USA, 14–19 July 2019.
38. Sotelo, L.D.; Hadidi, H.; Pratt, C.S.; Sealy, M.P.; Turner, J.A. Ultrasonic mapping of hybrid additively manufactured 420 stainless steel. *Ultrasonics* **2021**, *110*, 106269. [CrossRef]
39. Sotelo, L.D.; Karunakaran, R.; Pratt, C.S.; Sealy, M.P.; Turner, J.A. Ultrasound in situ characterization of hybrid additively manufactured Ti6Al4V. *J. Acoust. Soc. Am.* **2021**, *150*, 4452–4463. [CrossRef]
40. Aydogan, B.; O'Neil, A.; Sahasrabudhe, H. Microstructural and mechanical characterization of stainless steel 420 and Inconel 718 multi-material structures fabricated using laser directed energy deposition. *J. Manuf. Process.* **2021**, *68*, 1224–1235. [CrossRef]
41. Papadakis, E.P. The measurement of ultrasonic velocity. *Phys. Acoust.* **1990**, *19*, 81–106.

42. Bhatia, A.B. *Ultrasonic Absorption: An Introduction to the Theory of Sound Absorption and Dispersion in Gases, Liquids, and Solids*; Courier Corporation: Chelmsford, MA, USA, 1985.
43. Margetan, F.J.; Thompson, R.B.; Yalda-Mooshabad, I.; Han, Y.K. *Detectability of Small Flaws in Advanced Engine Alloys*; Iowa State University: Ames, IA, USA, 1993.
44. Panetta, P.D.; Bland, L.G.; Tracy, M.; Hassan, W. Ultrasonic backscattering measurements of grain size in metal alloys. In *TMS 2014: 143rd Annual Meeting & Exhibition*; Springer: Berlin/Heidelberg, Germany, 2014; pp. 723–730.
45. Sindhura, D.; Sravya, M.V.; Murthy, G. Comprehensive microstructural evaluation of precipitation in Inconel 718. *Metallogr. Microstruct. Anal.* **2019**, *8*, 233–240. [CrossRef]
46. Barnard, D.; Dace, G.; Buck, O. Acoustic harmonic generation due to thermal embrittlement of Inconel 718. *J. Nondestruct. Eval.* **1997**, *16*, 67–75. [CrossRef]
47. Chen, Y.; Lu, F.; Zhang, K.; Nie, P.; Hosseini, S.R.E.; Feng, K.; Li, Z. Dendritic microstructure and hot cracking of laser additive manufactured Inconel 718 under improved base cooling. *J. Alloys Compd.* **2016**, *670*, 312–321. [CrossRef]
48. Hassan, B.; Corney, J. Grain boundary precipitation in Inconel 718 and ATI 718Plus. *Mater. Sci. Technol.* **2017**, *33*, 1879–1889. [CrossRef]
49. Deng, D. Additively Manufactured Inconel 718: Microstructures and Mechanical Properties. Ph.D. Thesis, Linköping University, Linköping, Sweden, 2018.
50. Baicheng, Z.; Xiaohua, L.; Jiaming, B.; Junfeng, G.; Pan, W.; Chen-nan, S.; Muiling, N.; Guojun, Q.; Jun, W. Study of selective laser melting (SLM) Inconel 718 part surface improvement by electrochemical polishing. *Mater. Des.* **2017**, *116*, 531–537. [CrossRef]
51. Rossin, J.; Goodlet, B.; Torbet, C.; Musinski, W.; Cox, M.; Miller, J.; Groeber, M.; Mayes, A.; Biedermann, E.; Smith, S.; et al. Assessment of grain structure evolution with resonant ultrasound spectroscopy in additively manufactured nickel alloys. *Mater. Charact.* **2020**, *167*, 110501. [CrossRef]
52. Cazic, I.; Zollinger, J.; Mathieu, S.; El Kandaoui, M.; Plapper, P.; Appolaire, B. New insights into the origin of fine equiaxed microstructures in additively manufactured Inconel 718. *Scr. Mater.* **2021**, *195*, 113740. [CrossRef]
53. Stanke, F.E.; Kino, G.S. A unified theory for elastic wave propagation in polycrystalline materials. *J. Acoust. Soc. Am.* **1984**, *75*, 665–681. [CrossRef]
54. Arguelles, A.P.; Turner, J.A. Ultrasonic attenuation of polycrystalline materials with a distribution of grain sizes. *J. Acoust. Soc. Am.* **2017**, *141*, 4347–4353. [CrossRef] [PubMed]
55. Yang, L.; Lobkis, O.; Rokhlin, S. Shape effect of elongated grains on ultrasonic attenuation in polycrystalline materials. *Ultrasonics* **2011**, *51*, 697–708. [CrossRef] [PubMed]
56. Zhang, X.G.; Simpson, W., Jr.; Vitek, J.; Barnard, D.; Tweed, L.; Foley, J. Ultrasonic attenuation due to grain boundary scattering in copper and copper-aluminum. *J. Acoust. Soc. Am.* **2004**, *116*, 109–116. [CrossRef]
57. Liu, F.; Lin, X.; Leng, H.; Cao, J.; Liu, Q.; Huang, C.; Huang, W. Microstructural changes in a laser solid forming Inconel 718 superalloy thin wall in the deposition direction. *Opt. Laser Technol.* **2013**, *45*, 330–335. [CrossRef]
58. Li, Z.; Chen, J.; Sui, S.; Zhong, C.; Lu, X.; Lin, X. The microstructure evolution and tensile properties of Inconel 718 fabricated by high-deposition-rate laser directed energy deposition. *Addit. Manuf.* **2020**, *31*, 100941. [CrossRef]
59. Kumar, S.P.; Elangovan, S.; Mohanraj, R.; Ramakrishna, J. A review on properties of Inconel 625 and Inconel 718 fabricated using direct energy deposition. *Mater. Today Proc.* **2021**, *46*, 7892–7906. [CrossRef]
60. Parimi, L.L.; Ravi, G.; Clark, D.; Attallah, M.M. Microstructural and texture development in direct laser fabricated IN718. *Mater. Charact.* **2014**, *89*, 102–111. [CrossRef]
61. Zhai, Y.; Lados, D.A.; Brown, E.J.; Vigilante, G.N. Understanding the microstructure and mechanical properties of Ti-6Al-4V and Inconel 718 alloys manufactured by Laser Engineered Net Shaping. *Addit. Manuf.* **2019**, *27*, 334–344. [CrossRef]
62. Yeoh, Y.C.; Macchi, G.; Jain, E.; Gaskey, B.; Raman, S.; Tay, G.; Verdi, D.; Patran, A.; Grande, A.M.; Seita, M. Multiscale microstructural heterogeneity and mechanical property scatter in Inconel 718 produced by directed energy deposition. *J. Alloys Compd.* **2021**, *887*, 161426. [CrossRef]
63. Truell, R.; Elbaum, C.; Chick, B.B. *Ultrasonic Methods in Solid State Physics*; Academic Press: Cambridge, MA, USA, 2013.
64. Alers, G.; Thompson, D. Dislocation contributions to the modulus and damping in copper at megacycle frequencies. *J. Appl. Phys.* **1961**, *32*, 283–293. [CrossRef]
65. Granato, A.; Lücke, K. Theory of mechanical damping due to dislocations. *J. Appl. Phys.* **1956**, *27*, 583–593. [CrossRef]
66. Fergani, O.; Berto, F.; Welo, T.; Liang, S. Analytical modelling of residual stress in additive manufacturing. *Fatigue Fract. Eng. Mater. Struct.* **2017**, *40*, 971–978. [CrossRef]
67. Dike, J.; Johnson, G. Residual stress determination using acoustoelasticity. *J. Appl. Mech. Mar.* **1990**, *57*, 12–17. [CrossRef]
68. Rogers, P.H.; Van Buren, A.L. An exact expression for the lommeldiffraction correction integral. *J. Acoust. Soc. Am.***1974**, *55*, 724–728. [CrossRef]